

# Major groove width variations in RNA structures determined by NMR and impact of $^{13}\text{C}$ residual chemical shift anisotropy and $^1\text{H}$ – $^{13}\text{C}$ residual dipolar coupling on refinement

Blanton S. Tolbert · Yasuyuki Miyazaki · Shawn Barton ·  
Benyam Kinde · Patrice Starck · Rashmi Singh ·  
Ad Bax · David A. Case · Michael F. Summers

Received: 6 April 2010 / Accepted: 20 April 2010 / Published online: 15 June 2010  
© Springer Science+Business Media B.V. 2010

**Abstract** Ribonucleic acid structure determination by NMR spectroscopy relies primarily on local structural restraints provided by  $^1\text{H}$ – $^1\text{H}$  NOEs and J-couplings. When employed loosely, these restraints are broadly compatible with A- and B-like helical geometries and give rise to calculated structures that are highly sensitive to the force fields employed during refinement. A survey of recently reported NMR structures reveals significant variations in helical parameters, particularly the major groove width. Although helical parameters observed in high-resolution X-ray crystal structures of isolated A-form RNA helices are sensitive to crystal packing effects, variations among the published X-ray structures are significantly smaller than

those observed in NMR structures. Here we show that restraints derived from aromatic  $^1\text{H}$ – $^{13}\text{C}$  residual dipolar couplings (RDCs) and residual chemical shift anisotropies (RCSAs) can overcome NMR restraint and force field deficiencies and afford structures with helical properties similar to those observed in high-resolution X-ray structures.

**Keywords** NMR · RNA structure determination · Isotope labeling · Residual dipolar coupling · Residual chemical shift anisotropy

**Electronic supplementary material** The online version of this article (doi:10.1007/s10858-010-9424-x) contains supplementary material, which is available to authorized users.

B. S. Tolbert · Y. Miyazaki · S. Barton · B. Kinde · P. Starck ·  
R. Singh · M. F. Summers (✉)  
Howard Hughes Medical Institute and Department of Chemistry  
and Biochemistry, University of Maryland Baltimore County,  
1000 Hilltop Circle, Baltimore, MD 21250, USA  
e-mail: summers@umbc.edu

**Present Address:**  
B. S. Tolbert  
Department of Chemistry and Biochemistry, Miami University  
of Ohio, Oxford, OH 45056, USA

A. Bax  
Laboratory of Chemical Physics, NIDDK, National Institutes  
of Health, Bethesda, MD 20892, USA

D. A. Case (✉)  
Department of Chemistry & Chemical Biology and BioMaPS  
Institute, Rutgers University, 610 Taylor Road, Piscataway,  
NJ 08854-8087, USA  
e-mail: case@biomaps.rutgers.edu

## Introduction

Determination of ribonucleic acid structure by NMR spectroscopy can be challenging for a number of reasons. Limited  $^1\text{H}$  and  $^{13}\text{C}$  NMR chemical shift dispersion, resulting from the presence of only four primary nucleotides, can hinder signal assignments for RNAs of even modest sizes. Although spectral resolution can be improved through the use of multi-dimensional  $^{13}\text{C}$  editing, the aromatic  $^1\text{H}$  and  $^{13}\text{C}$  atoms critical for residue assignment and structure analysis exhibit strong  $^1\text{H}$ – $^{13}\text{C}$  dipolar coupling in larger RNAs, which can result in severely broadened NMR signals. As such, the average size of the 298 RNA NMR structures that have been deposited in the Nucleic Acid Database (<http://ndbserver.rutgers.edu/>) to date is only 25 nucleotides, and only 13 comprise more than 50 nucleotides.

An additional problem is that RNA structures solved by NMR are often experimentally underdetermined. Limited chemical shift dispersion of the  $^{31}\text{P}$  NMR signals generally precludes quantitative determination of phosphodiester torsion angles (although  $^{31}\text{P}$  chemical shifts are sometimes

used as a guide for applying model torsion angle restraints; Allain and Varani 1997; Zhou et al. 2001; Lukavsky and Puglisi 2005). Low overall proton density and few or no NOEs between elements of secondary structure are also problematic (Allain and Varani 1997; Lukavsky and Puglisi 2005), and since the majority of NOE-derived distance restraints typically involve protons in the major groove, RNA structures generated with simple force fields that lack electrostatic repulsion terms can exhibit unrealistically narrow major grooves (Rife et al. 1999; D'Souza et al. 2004). In addition, because the intra- and inter-residue NOE and torsion angle restraints are generally employed loosely (i.e., with flat distance limit potentials), they are usually broadly compatible with a wide range of A- and B-like helical geometries. Although the use of loose distance restraints works well for proteins, which have packing interactions that give rise to extensive long-range  $^1\text{H}$ – $^1\text{H}$  interaction networks, the distance uncertainties can lead to propagation errors for helical segments with only intra- and sequential-residue NOE restraints, and result in structures that are highly sensitive to the empirical force fields used during refinement (Rife et al. 1999; Zhou et al. 2001; D'Souza et al. 2004).

Orientation restraints derived from residual dipolar couplings (RDCs) can lead to improvement in the local and global precision of nucleic acid structures determined by NMR (Bayer et al. 1999; Mollova et al. 2000; Tjandra et al. 2000; Trantirek et al. 2000; Al-Hashimi et al. 2001a; Al-Hashimi et al. 2001b; Al-Hashimi et al. 2001c; Warren and Moore 2001; Al-Hashimi et al. 2002; Al-Hashimi and Patel 2002; Al-Hashimi et al. 2003; Lawrence et al. 2003; Lukavsky et al. 2003; D'Souza et al. 2004; Stefl et al. 2004; Walsh et al. 2004; Bax and Grishaev 2005; Lukavsky and Puglisi 2005; Walsh and Wang 2005; Al-Hashimi 2007; Wang et al. 2007; Ying et al. 2007; Al-Hashimi and Walter 2008; Latham et al. 2008; Zhang and Al-Hashimi 2008; Zuo et al. 2008; Fisher and Al-Hashimi 2009; Frank et al. 2009), and have been used to establish static and dynamic inter-helical orientations, as well as local structure (Mollova et al. 2000; Lukavsky et al. 2003; D'Souza et al. 2004; Davis et al. 2005; Staple and Butcher 2005; Zhang et al. 2006; Skrisovska et al. 2007; Ying et al. 2007; Zhang et al. 2007; Kim et al. 2008). Although structures generated with RDC restraints typically exhibit improved convergence, it has been difficult to quantitatively assess structural accuracy because X-ray crystal structures of isolated RNA helices are sensitive to crystal packing effects. For example, a 17-base RNA was shown to adopt four distinct sequence-independent but lattice-dependent conformations in a single crystal (Shah and Brunger 1999), in which the major groove widths (reported here as the mean distance between the phosphate P atoms of the (i) and (i+6) base pairs;  $d_{\text{P-P}}$ ) ranged from 9.4 to 13.8 Å.

Although quantitative comparison of individual RNA NMR and X-ray structures is problematic (Zhou et al. 2001), trends in published X-ray structures exist that have allowed us to qualitatively assess structures calculated using NMR-derived restraints. One notable observation is that the major groove widths of NMR structures reported for A-form helical RNAs are often well outside the ranges expected on the basis of high-resolution X-ray crystal structures. Here we show that aromatic  $^1\text{H}$ – $^{13}\text{C}$  RDC and  $^{13}\text{C}$  residual chemical shift anisotropy (RCSA) restraints, measured using high sensitivity  $^1\text{H}$ – $^{13}\text{C}$  “individual multiplet component” (IMC) experiments, can overcome restraint deficiencies associated with traditional NMR methods, as well as force field deficiencies, and afford structures with helical properties consistent with those observed in the surveyed X-ray crystal structures.

## Results and discussion

### Major groove width variations in NMR and X-ray structures

Helical properties (measured with the program 3DNA (Lu and Olson 2008)) and mean  $d_{\text{P-P}}$  distances (the average  $d_{\text{P-P}}$  distance measured for a given helical segment using pymol (DeLano 2002)) of six high resolution X-ray crystal structures that contain only standard Watson–Crick (WC) base pairs (resolution <2.5 Å), and of helical segments from the 2.4 Å structure of the 50S ribosomal subunit that only contain WC base pairs and no long-range base interactions, are summarized in Table 1 (see also Fig. 1). The X-ray structures exhibit mean  $d_{\text{P-P}}$  distances in the range of 8.8 Å (NDB ID 157D) to 12.6 Å (NDB 433D), with an average mean  $d_{\text{P-P}}$  of  $11.1 \pm 2.2$  Å. Major groove widths of 25 additional isolated helices that contain non-canonical base pairs and bulges, refined to high resolution by X-ray crystallography, have similar major groove widths (Fig. 1 and Supplementary Table S1). Cross-helix  $d_{\text{P-P}}$  distances were also measured for 72 A-form helical segments in NMR-derived RNA structures deposited in the RSCB Structure Databank from 2005 through 2009 (Supplementary Table S2). The NMR structures exhibit mean  $d_{\text{P-P}}$  distances in the range of 7.4 Å (NDB 2K66) to 28.6 Å (NDB 2H2X), with the average mean  $d_{\text{P-P}}$  distance being  $15.7 \pm 4.7$  Å (Fig. 1 and Table 1). The average, range, and maximum mean  $d_{\text{P-P}}$  values are significantly greater than those observed in the X-ray structures examined. We were unable to identify correlations between  $d_{\text{P-P}}$  values and the software package or type of experimental restraints employed that would explain the large variations among the NMR structures.

**Table 1** Helical parameters for representative high-resolution X-ray structures and ensembles of calculated [DIS]<sub>2</sub> NMR structures

	d <sub>p,p</sub>	Shift	Slide	Rise	Tilt	Roll	Twist	Propeller
X-ray structures (resolution)								
157D <sup>a</sup> (1.8)	8.8 ± 0.6	0.00 ± 0.6	-1.4 ± 0.3	3.3 ± 0.2	0.0 ± 4.2	10.1 ± 2.4	31.7 ± 5.7	-15.5 ± 6.7
1RNA <sup>b</sup> (2.25)	9.5 ± 1.6	0.0 ± 0.4	-1.3 ± 0.2	3.2 ± 0.3	-1.1 ± 3.6	9.7 ± 5.0	31.7 ± 4.6	-19.3 ± 3.7
1QC0 <sup>c</sup> (1.55)	10.6 ± 1.6	0.0 ± 0.4	-1.7 ± 0.5	3.2 ± 0.2	0.1 ± 1.9	8.0 ± 3.8	29.0 ± 10.8	-12.2 ± 3.4
1QCU <sup>c</sup> (1.2)	10.4 ± 1.1	0.0 ± 0.2	-0.7 ± 0.8	1.5 ± 1.6	8.5 ± 3.9	4.8 ± 4.4	21.1 ± 29.9	-14.3 ± 2.3
405D <sup>d</sup> (2.5)	10.7 ± 1.6	0.0 ± 0.3	-1.5 ± 0.2	3.3 ± 0.2	0.2 ± 2.1	9.5 ± 4.7	31.6 ± 5.8	-10.4 ± 4.4
433D <sup>e</sup> (2.1)	12.6 ± 0.9	0.1 ± 0.9	-1.7 ± 0.4	3.2 ± 0.2	0.2 ± 4.0	7.0 ± 4.0	31.1 ± 6.9	-9.6 ± 5.3
Ribosome <sup>f</sup> (2.4)	11.1 ± 2.4	0.0 ± 0.5	-1.6 ± 0.5	3.2 ± 0.2	0.4 ± 2.8	8.4 ± 4.7	31.5 ± 8.9	-8.0 ± 9.2
Mean ± SD <sup>g</sup>	11.1 ± 2.2	0.0 ± 0.6	-1.6 ± 0.5	3.2 ± 0.2	0.1 ± 2.8	8.2 ± 4.4	30.9 ± 9.0	-12.7 ± 3.9
[DIS] <sub>2</sub>								
Nucgen (Bansal et al. 1995)	10.0 ± 0.0	0.0 ± 0.0	-1.8 ± 0.0	3.4 ± 0.0	0.0 ± 0.1	8.9 ± 0.2	31.4 ± 0.9	13.7 ± 0.0
Nucgen+Amber	14.7 ± 0.2	0.0 ± 0.1	-1.7 ± 0.1	3.3 ± 0.1	0.0 ± 1.1	6.2 ± 4.0	30.3 ± 2.1	-13.7 ± 1.2
Cyana								
NOE	6.6 ± 1.2	0.0 ± 0.2	-1.2 ± 0.2	3.5 ± 0.1	0.0 ± 0.9	16.1 ± 4.3	30.3 ± 1.3	-9.9 ± 3.2
NOE+RDC	12.5 ± 0.5	0.0 ± 0.2	-1.3 ± 0.2	3.3 ± 0.4	0.1 ± 2.4	10.0 ± 7.6	31.6 ± 1.6	-12.1 ± 5.6
Amber								
No exper restr <sup>h</sup>	13.9 ± 0.3	0.0 ± 0.1	-1.9 ± 0.2	3.3 ± 0.1	0.0 ± 1.6	7.0 ± 3.2	29.7 ± 1.9	-10.6 ± 1.6
NOE	13.6 ± 0.3	0.0 ± 0.1	-1.9 ± 0.1	3.3 ± 0.1	0.0 ± 1.2	7.6 ± 3.6	30.7 ± 1.8	-11.8 ± 2.0
NOE+RDC <sup>i</sup>	12.1 ± 0.3	0.0 ± 0.2	-1.8 ± 0.1	3.2 ± 0.2	0.0 ± 2.4	8.7 ± 5.7	31.1 ± 2.0	-15.0 ± 5.4
NOE+RCSA <sup>j</sup>	11.6 ± 0.1	0.0 ± 0.1	-1.9 ± 0.1	3.3 ± 0.1	0.0 ± 0.6	6.7 ± 4.3	30.8 ± 1.7	-11.6 ± 2.6
NOE+RDC+RCSA <sup>k</sup>	11.2 ± 0.2	0.0 ± 0.2	-1.7 ± 0.2	3.3 ± 0.2	0.0 ± 1.7	10.2 ± 4.9	30.9 ± 2.7	-18.1 ± 5.2
10% E <sub>elec</sub> <sup>l</sup>								
No exper restr <sup>h</sup>	4.6 ± 0.3	0.0 ± 0.1	-1.6 ± 0.2	3.2 ± 0.1	0.0 ± 1.3	15.2 ± 4.0	30.9 ± 3.4	-16.4 ± 2.8
NOE	4.5 ± 0.2	0.0 ± 0.1	-1.6 ± 0.1	3.2 ± 0.1	0.0 ± 1.1	14.7 ± 3.7	31.2 ± 2.9	-15.8 ± 2.8
NOE+RDC <sup>i</sup>	10.8 ± 0.2	0.0 ± 0.2	-1.6 ± 0.1	3.2 ± 0.2	0.0 ± 2.5	8.9 ± 4.4	31.6 ± 2.5	-18.5 ± 5.5
NOE+RCSA <sup>j</sup>	10.7 ± 0.2	0.0 ± 0.1	-1.7 ± 0.1	3.2 ± 0.1	0.0 ± 1.0	8.1 ± 2.7	31.9 ± 1.8	-17.6 ± 4.0
NOE+RDC+RCSA <sup>k</sup>	9.7 ± 0.3	0.0 ± 0.2	-1.5 ± 0.2	3.2 ± 0.2	0.0 ± 2.3	10.4 ± 3.7	31.8 ± 3.2	-21.5 ± 5.7
200% E <sub>elec</sub> <sup>m</sup>								
No exper restr <sup>h</sup>	16.3 ± 0.9	0.0 ± 0.3	-2.0 ± 0.3	3.5 ± 0.1	0.0 ± 2.5	7.4 ± 4.9	28.8 ± 2.3	-9.0 ± 4.2
NOE	14.4 ± 1.1	0.0 ± 0.2	-1.9 ± 0.2	3.4 ± 0.1	0.0 ± 1.4	8.7 ± 4.5	30.4 ± 2.3	-9.2 ± 2.8
NOE+RDC+RCSA <sup>k</sup>	12.4 ± 1.0	0.0 ± 0.2	-1.5 ± 0.2	3.2 ± 0.2	0.0 ± 2.3	10.3 ± 3.7	31.8 ± 2.9	-21.6 ± 5.4

d<sub>p,p</sub> (distance between the P atom of residue (i) and the cross-strand P atom of base pair (i+6)) and all other helical parameters measured with pymol (DeLano 2002) and 3DNA (Lu and Olson 2008), respectively; reported as mean ± std. dev

<sup>a</sup> Leonard et al. (1994)

<sup>b</sup> Dock-Bregeon et al. (1989)

<sup>c</sup> Klosterman et al. (1999)

<sup>d</sup> Pan et al. (1998)

<sup>e</sup> Trikha et al. (1999)

<sup>f</sup> Calculated for seven A-form helical segments extracted from the 50S ribosome structure that exclusively contain Watson-Crick base pairs: (H1 r12–21:r522–531, H2 r539–548:r608–617, H3 r646–658:r747–759, H4 r780–788:r858–866, H5 r1045–1054:r1060–1069, H6 r1138–1147:r1216–1225, H7 r2381–2389:r2399–2407; Klein et al. (2004)

<sup>g</sup> Statistics generated using all individual d<sub>p,p</sub> and base step measurements

<sup>h</sup> Cyana structures minimized using the GB force field with only chirality and H-bond restraints

<sup>i</sup> RDCs used as restraints for simultaneous calculation of structure and alignment tensor

<sup>j</sup> Structures calculated using a fixed alignment tensor derived from the NOE+RDC+RCSA calculations

<sup>k</sup> RDCs and RCSAs used as restraints for simultaneous calculation of structure and alignment tensor

<sup>l</sup> Electrostatic term (E<sub>elec</sub>) in the Amber force field reduced to 10% of the standard value

<sup>m</sup> E<sub>elec</sub> increased to 200% of the standard value

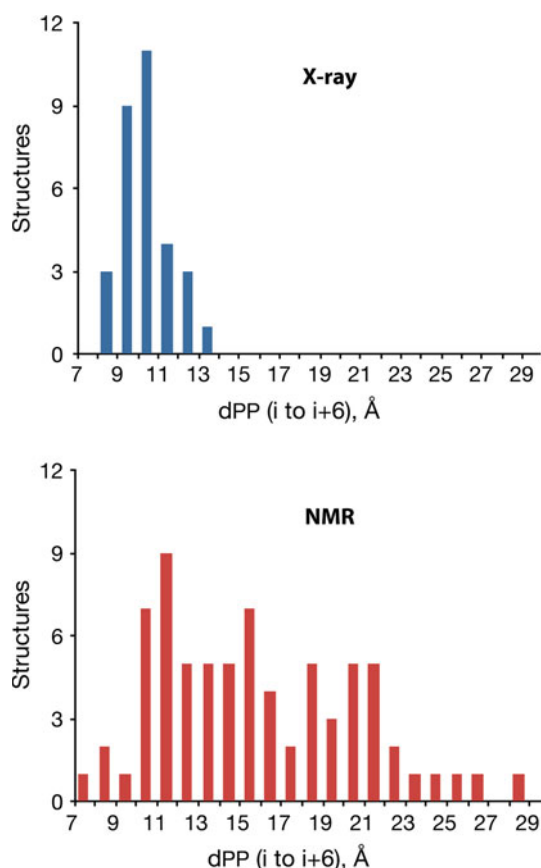


**Fig. 1** Plots showing mean  $d_{P-P}$  distances (average of the cross-major groove distances between the P atoms of base pairs (i) and (i+6)) of X-ray and NMR structures deposited in the RNA structure database. **a** X-ray structures (<2.5 Å resolution) of unmodified, A-form helical RNAs, including those with non-canonical base pairs (Table 1 and Suppl. Table S1), **b** NMR structures of A-form helical RNAs deposited from 2005 through 2009 (Suppl. Table S2)

### Measurement of $^1\text{H}$ – $^{13}\text{C}$ RDCs and $^{13}\text{C}$ RCSAs

Orientation information derived from RDCs and RCSAs offer a potential means for assessing and refining RNA structures, but the measurement of these values for larger RNAs can be problematic. The downfield components of the  $^{13}\text{C}$ – $\{^1\text{H}\}$  multiplet have relatively long relaxation times due to interference between the  $^{13}\text{C}$  chemical shift anisotropy (CSA) and heteronuclear dipolar relaxation mechanisms (Werbelow and Grant 1977; Gueron et al. 1983; the TROSY (Tr) effect (Pervushin et al. 1997)), and can be readily detected even for larger RNAs. However, the upfield anti-TROSY (anti-Tr) components exhibit more rapid  $T_2$  relaxation, a problem that is exacerbated for aromatic groups due to the strong  $^1\text{H}$ – $^{13}\text{C}$  dipolar interaction (Brutscher et al. 1998) to the extent of precluding RDC measurement (D'Souza et al. 2004). We implemented an approach that involves measurement of only the Tr- $^{13}\text{C}$  component (Grishaev et al. 2006). The  $^{13}\text{C}$  frequency shift

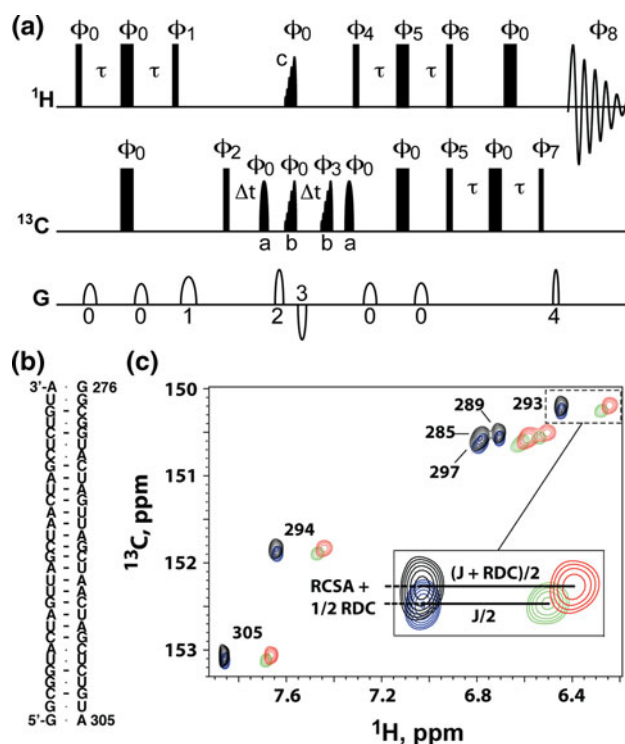


**Fig. 2** **a**  $^1\text{H}$ – $^{13}\text{C}$  IMC pulse sequence used for selective observation of the Tr( $^1\text{H}$ )–Tr( $^{13}\text{C}$ ) component of purine and pyrimidine aromatic  $^1\text{H}$ – $^{13}\text{C}$  multiplets. Decoupling during the evolution period (incremented at  $\Delta t$ ) is achieved using broad band hyperbolic secant (**a** 1.33 ms; 13.5 kHz bandwidth) and selective IBURP (Green and Freeman 1991; **b** 2.67 ms, 1.69 kHz bandwidth; **c** 1.33 m, 3.37 kHz bandwidth) inversion pulses;  $\tau = 1/4 J = 1.2$  ms. Phases for collection of the Tr( $^1\text{H}$ )–Tr( $^{13}\text{C}$ ) component are:  $\phi_{0,7} = x$ ,  $\phi_{1,5} = y$ ,  $\phi_2 = x,x,-x,-x$ ;  $\phi_3 = x,y$ ;  $\phi_4 = y$ ;  $\phi_6 = -x$ ;  $\phi_8 = x,-x,-x,x$ .  $\phi_7$  was empirically adjusted ( $-38^\circ$  in all experiments) to balance the effect of differential relaxation rates of single and multiple quantum coherence. Other components are collected using the following phases: anti-Tr( $^1\text{H}$ )–Tr( $^{13}\text{C}$ ):  $\phi_7 = -x$ ; Tr( $^1\text{H}$ )–anti-Tr( $^{13}\text{C}$ ):  $\phi_{1,4} = -y$ ; anti-Tr( $^1\text{H}$ )–anti-Tr( $^{13}\text{C}$ ):  $\phi_7 = -x$ ;  $\phi_{1,4} = -y$ . Echo-Antiecho quadrature detection is achieved by incrementing the phase  $\phi_7$  and  $\phi_8$  by 180 degrees and reversing the signs of gradients 2 and 3. The selective  $^1\text{H}$  IBURP pulse was only used for detection of pyrimidine  $\text{C}_5$ – $\text{H}_5$  and  $\text{C}_6$ – $\text{H}_6$  signals, and was centered at the non-observed aromatic proton frequency. Relative pulsed field gradient (PFG) strengths (sine shapes): G0, 500  $\mu\text{s}$ , 31%; G1, 400  $\mu\text{s}$ , 41%; G2 200  $\mu\text{s}$ , 50%; G3, 200  $\mu\text{s}$ ,  $-50\%$ ; G4, 100  $\mu\text{s}$ , 50%. **b** Nucleotide sequence and secondary structure of [DIS]<sub>2</sub>. **c** Portions of the RPCSA (blue, black) and Tr( $^{13}\text{C}$ )–Tr( $^1\text{H}$ ) IMC (red, green) spectra obtained for [A,G( $^{13}\text{C}$ )-DIS]<sub>2</sub> in the absence (blue, green) and presence (black, red) of Pfl phage. Inset Relationship between RDC and RPCSA

of this component that occurs upon partial molecular alignment (induced by the presence of alignment media such as Pfl phage (Hansen et al. 1998)) results from a combination of RDC and residual chemical shift anisotropy (RCSA) and is referred to as the residual pseudo-chemical shift anisotropy, or RPCSA. RPCSAs can be used directly as refinement restraints (Grishaev et al. 2006), but their values can result from significantly different combinations

of RDCs and RCSAs (Bryce et al. 2005; Grishaev et al. 2006), and it is therefore advantageous to employ the actual RCSA and RDC values as restraints for structure refinement.

RDCs were determined by measuring the frequency differences observed in spectra obtained using  $^{13}\text{C}$ -decoupled RPCSA (Grishaev et al. 2006; Ying et al. 2006) and Individual Multiplet Component (IMC) experiments. IMC spectra were obtained using the protocol of Andersson et al. (Andersson et al. 1998), optimized for detection of  $^1\text{H}$ - $^{13}\text{C}$  correlations in the nucleobases of uniformly  $^{13}\text{C}$  enriched nucleic acids (Grishaev et al. 2006; Ying et al. 2006), and including the use of field gradients for coherence selection (Fig. 2a). As discussed by Andersson et al. for backbone amide signals in proteins, recording separately the signals for the four combinations of  $\phi_4 = \pm y$  and  $\phi_7 = \pm x$ , these signals can be combined post acquisition to yield spectra displaying any one of the four  $^1\text{H}$ - $^{15}\text{N}$  two-dimensional doublet components (Andersson et al. 1998). For the application to  $^{13}\text{C}$ , where the Boltzmann component of  $^{13}\text{C}$  magnetization and the component transferred from the base  $^1\text{H}$  are comparable in magnitude, we find it beneficial to record the TROSY and anti-TROSY  $^{13}\text{C}$ - $\{^1\text{H}\}$  doublet components separately, with the  $\phi_1$  phase adjusted such that the Boltzmann  $^{13}\text{C}$  magnetization adds to the selected  $^{13}\text{C}$ - $\{^1\text{H}\}$  doublet component. Individual multiplet components are selected using appropriate phase cycling combinations given in the Fig. 2 caption.

$^1\text{H}$ - $^{13}\text{C}$  RDCs and  $^{13}\text{C}$  RPCSAs were measured for a  $^{13}\text{C}$ -isotopically labeled 60 nt RNA duplex corresponding to the dimer initiation site of the Moloney Murine Leukemia Virus (MLV; [DIS]<sub>2</sub>; Fig. 2b). Representative  $\text{Tr}(^1\text{H})$ - $\text{Tr}(^{13}\text{C})$ -IMC and RPCSA spectra obtained for samples prepared in the presence and absence of Pf1 phage are shown in Fig. 2c. RCSA values were calculated using the relationship:  $\text{RCSA} = \text{RPCSA} - \frac{1}{2} \text{RDC}$ . Although the RDC value could be measured from the shift in the  $^1\text{H}$  dimension of the TROSY component alone (as a function of added phage), in practice it is better to use the  $^{13}\text{C}$ -decoupled RPCSA spectra as a reference since the  $^1\text{H}$  NMR chemical shifts are sometimes slightly affected by the presence of alignment media. Under the experimental conditions employed (16 mg/ml Pf1 phage), RDC and RCSA values clustered in the range of 28.4 to 49.4 Hz and -136.6 to -262.6 ppb, respectively (Supplementary Table S3).

#### Influence of the force field and NOE restraints on RNA structure refinement

2D NOESY and TOCSY cross peak patterns and intensities observed for self-complementary residues C283–G298 of [DIS]<sub>2</sub> were consistent with an A-form helical

conformation (Wüthrich 1986; D'Souza et al. 2001). Moderate-to-strong intensity  $\text{H1}'$ -to- $\text{H2}'$  TOCSY cross peaks observed for residues G276–A282 and C299–A305 indicate that these residues partially populate a  $\text{C}_2'$ -endo conformation. Since all but two of these residues participate in non-canonical base pairing, and because  $^{13}\text{C}$  CSA tensors have only been determined for nucleotides in standard Watson-Crick base pairs (Hansen and Al-Hashimi 2006; Ying et al. 2006), G276–A282 and C299–A305 were not included in the following structural analysis.

[DIS]<sub>2</sub> structures were generated initially with Cyana (Güntert et al. 1997) using conservative NOE-derived distance restraints (see “Experimental” section). H-bond restraints based on NOE cross peak patterns observed for samples in D<sub>2</sub>O and 90% H<sub>2</sub>O/10% D<sub>2</sub>O solutions, and loose torsion angle restraints (flat potential bounds of  $\pm 50^\circ$ ) centered around A-form values (but wide enough to allow B-like geometries;  $\alpha = -62^\circ$ ,  $\beta = 180^\circ$ ,  $\gamma = 48^\circ$ ,  $\delta = 83^\circ$ ,  $\varepsilon = -152^\circ$ ,  $\zeta = -73^\circ$ ; Saenger 1984) were employed during the Cyana calculations (but not the subsequent Amber (Case et al. 2005) calculations; see below).

A total of 20 [DIS]<sub>2</sub> structures with lowest target functions was selected from an ensemble of 200 initial structures for analysis and refinement (Fig. 3a and Table 2). The helical properties of the Cyana structures were generally consistent with those expected for A-form helices, except that the cross-helix  $d_{p,p}$  distances were smaller than expected (mean  $d_{p,p} = 6.6 \pm 1.2 \text{ \AA}$ ) and the Roll values were relatively large ( $16.1 \pm 4.3^\circ$ ; Table 1). This is due to the fact that all but a few of the NOE-derived distance restraints involve protons in the major groove of the RNA, which in the absence of inter-phosphate repulsion terms

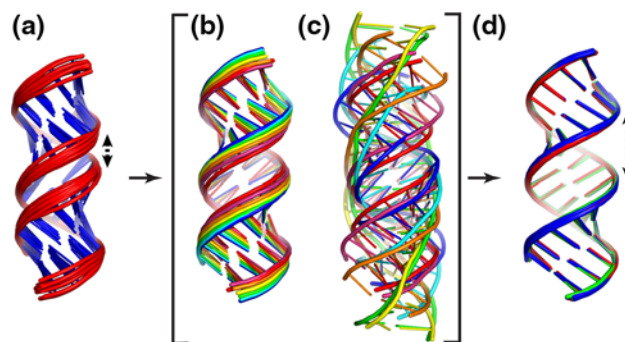


**Fig. 3** **a** Superposition of 20 [DIS]<sub>2</sub> Cyana structures, from 200 total, generated using loose NOE, hydrogen bond, and backbone torsion angle restraints. **b–d** MD simulations with Amber using NOE-derived distance, hydrogen bond, and planarity/chirality restraints (trajectory snapshots for MD simulations conducted at 0 and 300 K are shown in **b** and **c**, respectively) result in an expansion of the major groove, with  $d_{p,p}$  distances (dashed arrows) increasing from  $6.6 \pm 1.2 \text{ \AA}$  to  $13.6 \pm 0.3 \text{ \AA}$ . **d** Superposition of Cyana structures after refinement with Amber using only chirality and H-bond restraints (by minimization (blue) or annealing followed by minimization (green)) and upon inclusion of NOE-derived distance restraints (red)

**Table 2** NMR Restraints and Structure Statistics

Cyana <sup>a</sup>					
NOE-derived restraints					
Intraresidue					160
Sequential					122
Long range ( $ i - j  > 1$ )					21
H-bond restraints <sup>b</sup>					152
NOE restraints/residue					14.0
Total restraints/residue					23.4
Target funct. ( $\text{\AA}^2$ ) <sup>c</sup>					$0.025 \pm 0.000$
Upper dist. viol. ( $\text{\AA}$ ) <sup>c</sup>					$0.005 \pm 0.000$
Lower dist. viol. ( $\text{\AA}$ ) <sup>c</sup>					$0.001 \pm 0.000$
Sum VDW viol. ( $\text{\AA}$ ) <sup>c</sup>					$0.05 \pm 0.00$
RMSD ( $\text{\AA}$ ) <sup>d</sup>					$2.72 \pm 0.32$
Amber <sup>e</sup>	No exper restraints	NOE	NOE+RDC <sup>f</sup>	NOE+RCSA <sup>g</sup>	NOE+RDC <sup>f</sup> +RCSA <sup>g</sup>
AMB energy	−6,826.7 (1.1)	−6,827.7 (1.5)	−6,810.8 (2.2)	−6,825.7 (1.5)	−6,796.7 (1.1)
Distance	NA	1.59 (0.56)	2.58 (1.21)	1.96 (1.19)	3.68 (1.19)
Torsion	NA	0.22 (0.01)	1.19 (0.02)	1.31 (0.03)	6.67 (0.03)
RDC	NA	NA	2.62 (0.06)	NA	5.61 (0.11)
RCSA	NA	NA	NA	15.30 (0.58)	19.00 (0.27)
RMSD ( $\text{\AA}$ ) <sup>h</sup>	0.15	0.15	0.12	0.12	0.11
<i>10% E<sub>elec</sub><sup>i</sup></i>					
AMB energy	−342.0 (4.8)	−341.6 (0.2)	−323.4 (0.2)	−326.6 (0.3)	−324.1 (0.2)
Distance	8.07 (0.30)	8.80 (0.03)	10.12 (0.08)	8.53 (0.08)	12.78 (0.08)
Torsion	0.15 (0.01)	0.17 (0.01)	0.84 (0.02)	2.11 (0.05)	6.45 (0.04)
RDC	NA	NA	1.49 (0.04)	NA	3.08 (0.05)
RCSA	NA	NA	NA	13.03 (0.13)	14.47 (0.13)
RMSD ( $\text{\AA}$ ) <sup>h</sup>	0.04	0.05	0.06	0.12	0.05

Structure calculations and all statistics are for residues C283–G298. Molprobability clash scores for all Cyana and Amber structures were 0.0 (100th percentile)

<sup>a</sup> Statistics for 20 lowest-target function structures (from 200 structures generated)

<sup>b</sup> Four restraints per H-bond

<sup>c</sup> Reported as mean (standard deviation)

<sup>d</sup> Mean  $\pm$  standard deviation for all heavy atoms, relative to mean atom coordinates, calculated with Cyana

<sup>e</sup> Total of 42 RDC restraints

<sup>f</sup> Total of 36 RCSA restraints

<sup>g</sup> Energies reported in units of kCal/mol (std. dev. in parentheses)

<sup>h</sup> Mean for all heavy atoms, relative to mean atom coordinates, calculated with Suppose (Amber)

<sup>i</sup> Electrostatic term in the Amber ff99 force field reduced to 10% of the standard value

statistically biases the major groove protons toward a more collapsed structure (Rife et al. 1999; D'Souza et al. 2004).

The Cyana structures were then subjected to minimization with Amber (Case et al. 2005). In one calculation, the Amber force field (ff99 with Generalized Born (GB) solvent continuum parameters) was employed, along with loose hydrogen bond restraints to prevent fraying in subsequent high-temperature MD simulations and tight covalent geometry (chirality) restraints to prevent distortion of

covalent bond geometries that can occur during restrained MD simulations. In a second calculation, the NOE-derived  $^1\text{H}$ – $^1\text{H}$  distance restraints were included. Minimization by MD simulation at 0 K using only the Amber force field resulted in a significant expansion of the major groove, with  $d_{P-P}$  values increasing from  $6.6 \pm 1.2 \text{ \AA}$  to  $13.9 \pm 0.3 \text{ \AA}$  and the Roll between base pairs decreased from  $16.1 \pm 4.3^\circ$  to  $7.0 \pm 4.2^\circ$  (Table 1 and Fig. 3b, d). Essentially identical results were obtained when minimizations were performed

using the NOE-derived distance restraints, and also when minimization was preceded by MD simulations at 300 K (Fig. 3c, d).

Similar results were also obtained when an idealized [DIS]<sub>2</sub> model, generated with Nucgen (Bansal et al. 1995), was subjected to low-temperature MD annealing. Although the  $d_{p,p}$  distances in the initial Nucgen models (10.0 Å) were typical of those observed in X-ray structures, the propeller twists were opposite to experimentally observed values (Table 1). Minimization of the Nucgen models with Amber using only chirality and H-bond restraints resulted in structures indistinguishable from those obtained upon restrained MD refinement of the Cyana structures (Table 1). These findings indicate that (a) structures generated with Cyana using loose NOE-derived distance, torsion angle, and hydrogen bond restraints have relatively narrow major grooves and large Roll angles, (b) refinement of the Cyana structures using the standard Amber force field affords structures that are more consistent with the high-resolution X-ray structures, except that the major grooves are  $\sim 2$  Å wider than expected, (c) the NOE restraints, as applied loosely, are compatible with a broad range of Roll and  $d_{p,p}$  values, and (d) the Amber force field, and not the refinement strategy or restraints, is responsible for the structural changes that occur upon refinement.

### Influence of RDC and RCSA restraints on structure refinement

The RDCs and RCSAs measured for [DIS]<sub>2</sub> were then fitted to the Cyana, Amber-only, and Amber-NOE refined structures by least squares minimization of the alignment tensor using Amber (Fig. 4). Nearly identical fits were obtained with RAMAH (Hansen and Al-Hashimi 2006; see “Methods” section for details). Significantly better fits were obtained for the Amber-refined structures compared to the Cyana structures (Fig. 4), indicating that refinement with Amber (with or without the NOE restraints) leads to conformers that more accurately reflect the solution-state structure.

MD refinement of the Amber-NOE structures using the RDC restraints (conducted in a manner in which both the atomic coordinates and alignment tensor were simultaneously optimized) led to a significant narrowing of the major groove, with  $d_{p,p}$  values decreasing from  $13.6 \pm 0.3$  to  $12.1 \pm 0.3$  Å (Fig. 5a and Table 1). Refinement of the Amber-NOE structures using the RCSA restraints (but not RDCs) also resulted in a narrowing of the major groove ( $d_{p,p} = 11.6 \pm 0.1$  Å; Fig. 5b and Table 1). These calculations were conducted using a fixed alignment tensor obtained from calculations that fitted both the RDC and RCSA data (see below), and although good agreement was

**Fig. 4** Plots of molecular superpositions (top) and experimental (vertical) versus back-calculated (horizontal) RDC (black) and RCSA (red) data in Hz (bottom) for representative [DIS]<sub>2</sub> structures calculated with Cyana and refined with Amber. To facilitate comparisons, the horizontal line has a slope of 1.0. Pearson ( $P$ ) and correlation coefficient ( $R^2$ ) statistics for the experimental vs. calculated data are also shown. **a** Cyana structures generated using NOE-derived distance and H-bond restraints. **b, c** Amber structures generated by MD refinement of the Cyana structures **b** using only the ff99 force field with GB solvent simulation and no additional restraints, and **c** using NOE-derived distance, H-bond and chirality restraints

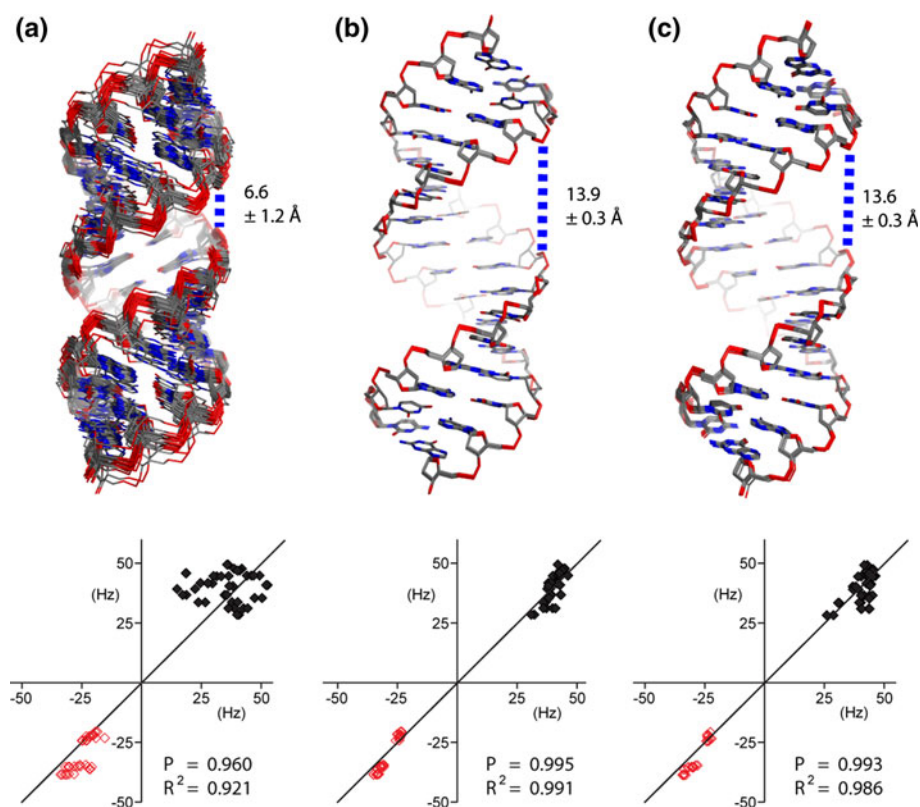


**Fig. 5** Plots of molecular superpositions (*top*) and representative experimental (*vertical*) versus back-calculated (*horizontal*) RDC (*black*) and RCSA (*red*) data (*bottom*) for 20 Amber structures after minimization using **a** NOE+RDC restraints, **b** NOE+RCSA restraints (with a fixed alignment tensor—see text), and **c** NOE+RDC+RCSA restraints. The starting structures for all three sets of calculations are shown in Fig. 3c, and all calculations led to reductions in major groove widths to values consistent with high-resolution RNA X-ray structures. The horizontal line is plotted with a slope of 1.0, and Pearson (*P*) and *R*<sup>2</sup> values are shown

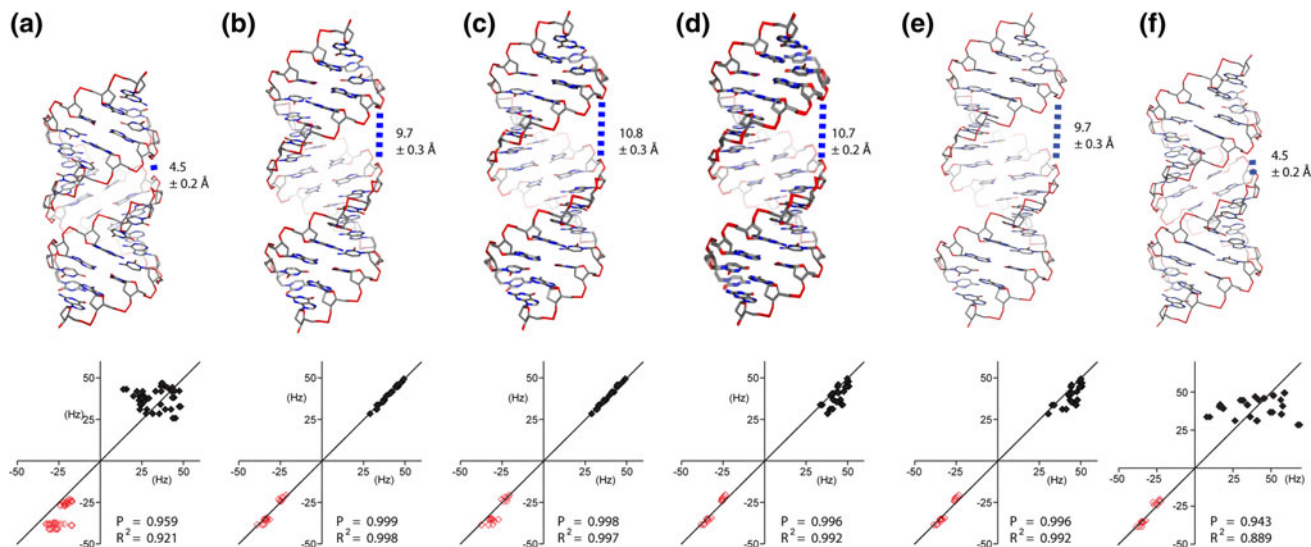
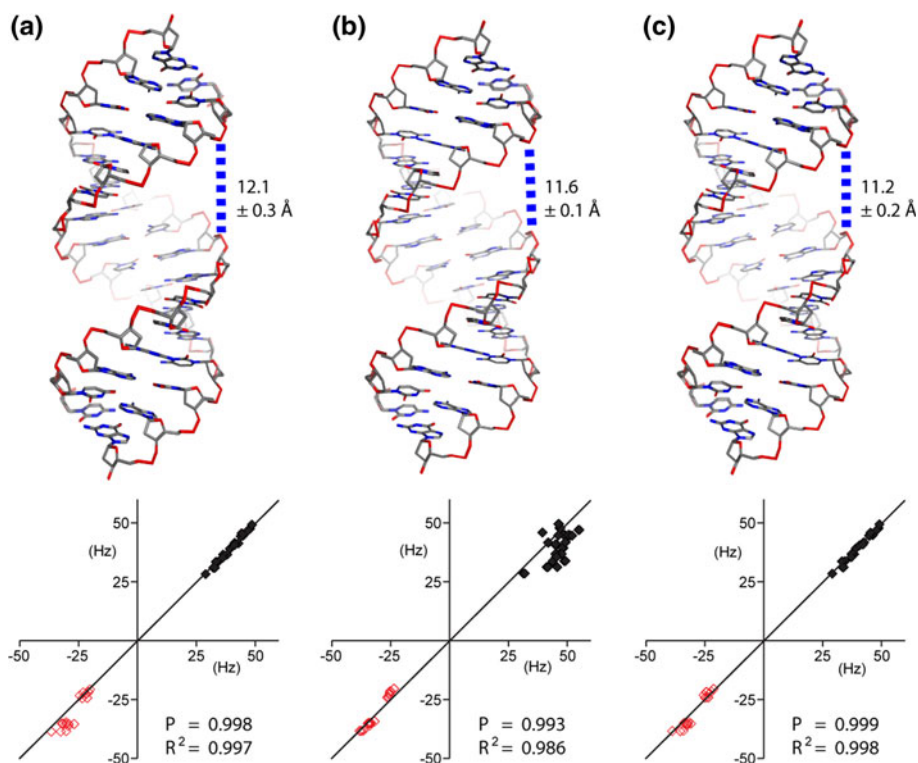


**Fig. 6** **a–d** Plots of molecular superpositions (*top*) and representative experimental (*vertical*) versus back-calculated (*horizontal*) RDC (*black*) and RCSA (*red*) data (*bottom*) for [DIS]<sub>2</sub> RNA structures refined with Amber using a modified GB force field in which the electrostatic term was reduced to 10% of the normal value. The 20 initial Cyana structures (Fig. 4a) were refined using the following restraint combinations: **a** NOE-only; **b** NOE+RDC+RCSA; **c** NOE+RDC; **d** NOE+RCSA (with fixed alignment tensor). **e, f** Representative structures obtained upon simultaneous refinement

of the atomic coordinates and orientation tensor using only the NOEs and RCSAs as restraints. Although both structures and their corresponding alignment tensors are compatible with the RCSA data, the predicted alignment tensor for **f** is highly asymmetric and incompatible with both the calculated rotational diffusion tensor and the experimental RDCs (see Table 3). These findings illustrate the potential limitations of using RCSAs alone for simultaneous structure/tensor calculations (see text for details)

observed between the experimental and back-calculated RCSAs, the RDCs agreed less favorably with the back-calculated values (Fig. 5b). MD simulations performed

using both RDC and RCSA restraints afforded structures with major groove widths ( $d_{p-p} = 11.2 \pm 0.2 \text{ \AA}$ ) similar to those obtained using only RDC or RCSA restraints (Fig. 5c

and Table 1), and as expected, these structures exhibited the best agreement between the experimental and back-calculated RDCs and RCSAs (Fig. 5c). The average of the Roll values increased upon inclusion of the RDC and RCSA restraints, but the individual Roll values were well within the limits of the wide range of values observed in the X-ray structures (as evidence by the large standard deviation values shown in Table 1). Although the Cyana software package does not allow for inclusion of RCSA restraints, refinement with Cyana using only the RDC restraints using a gridsearch approach also afforded structures with a wider major groove ( $d_{p,p} = 12.5 \pm 0.5 \text{ \AA}$ ; Table 1).

#### RDC and RCSA restraints can overcome more severe force field deficiencies

The above results indicate that the standard Amber force field favors RNA helices with major groove widths that are ca. 2 Å larger than those observed in high resolution X-ray crystal structures; that loosely applied NOE restraints do not correct for the wider major groove of the Amber structures or the narrower groove of the Cyana structures; and that orientation restraints derived from limited  $^1\text{H}$ – $^{13}\text{C}$  RDC and  $^{13}\text{C}$  RCSA measurements induce the formation of structures with major groove widths that are more consistent with those observed in the surveyed X-ray crystal structures. As a test for the ability of orientation restraints to overcome more severe force field deficiencies, structure refinements were conducted as described above, except that the electrostatic term in the Amber force field ( $E_{\text{elec}}$ ) was reduced to 10% of the normal value. Minimization of the 20 Cyana starting structures with this modified force field, with inclusion of the NOE, H-bond and chirality restraints, led to a nearly complete collapse of the major groove ( $d_{p,p} = 4.5 \pm 0.2 \text{ \AA}$ ), and back-calculated RDC and RCSA values were in poor agreement with experimental values (Fig. 6a).

The above structures were then subjected to low-temperature annealing ( $T = 50 \text{ K}$ ) and minimization using the RDCs and RCSAs as restraints. All other force field parameters were the same as those applied above, including the 90% reduction in the  $E_{\text{elec}}$  term. As shown in Fig. 6b, implementation of these restraints led to an expansion of the major groove, with  $d_{p,p}$  values ( $9.7 \pm 0.3 \text{ \AA}$ ) approaching those obtained when the standard Amber force field was employed and within the range of values observed in high-resolution X-ray crystal structures (Table 1). Refinement using only the RDC restraints, conducted in a manner in which the alignment tensor and structure were simultaneously optimized, led to structures with slightly larger major grooves ( $d_{p,p} = 10.8 \pm 0.3 \text{ \AA}$ ; Fig. 6c and Table 1). Similar results were obtained using

only the RCSA restraints, although these calculations were conducted using a fixed alignment tensor generated previously from the RDC+RCSA calculations ( $d_{p,p} = 10.7 \pm 0.2 \text{ \AA}$ ; Fig. 6d and Table 1).

As a final test, the Cyana structures were minimized as described above using an Amber force field in which the  $E_{\text{elec}}$  term was doubled relative to the standard value. Structures refined without NOE or orientation restraints (but including chirality and H-bond restraints) exhibited very wide major grooves ( $d_{p,p} = 16.3 \pm 0.9 \text{ \AA}$ ; Table 1). Refinement with the NOE restraints resulted in a significant reduction in the major groove width ( $d_{p,p} = 14.4 \pm 1.1 \text{ \AA}$ ), and inclusion of RDC and RCSA restraints led to further reduction, with  $d_{p,p}$  values ( $12.4 \pm 1.0$ ) in the

**Table 3** Alignment tensors for representative  $[\text{DIS}]_2$  structures

Structure	$A_a$	$A_r$	$E_{\text{RDC}}$	$E_{\text{RCSA}}$
Cyana				
NOE <sup>a</sup>	124.3	1.3	658.5	175.8
NOE+RDC <sup>b</sup>	112.5	0.1	5.1	NA
Amber				
No Exper. Restr <sup>a</sup>	104.4	1.05	78.7	53.0
NOE <sup>a</sup>	104.2	0.46	115.1	46.1
NOE+RDC <sup>c</sup>	109.2	1.9	2.7	NA
NOE+RDC+RCSA <sup>d</sup>	125.3	0.6	5.5	18.7
NOE+RCSA <sup>e</sup>	114.6	7.5	NA	15.3
GB (10% $E_{\text{elec}}$ )				
No Exp. Restr <sup>a</sup>				
NOE <sup>a</sup>	127.6	0.8	706.5	214.9
NOE+RDC <sup>c</sup>	116.7	1.4	1.5	NA
NOE+RDC+RCSA <sup>d</sup>	133.4	0.9	3.0	14.3
NOE+RCSA <sup>e,f</sup>	119.8	1.1	NA	13.1
NOE+RCSA <sup>e,f</sup>	149.8	30.2	NA	13.7

Axial ( $A_a$ ) and rhombic ( $A_r$ ) components of the Saupe alignment tensor ( $\times 10^5$ ) and penalty functions for the RDC and RCSA terms ( $E_{\text{RDC}}$  and  $E_{\text{RCSA}}$ , respectively; kcal/mol) after minimization with Amber

<sup>a</sup> Back-calculated values for structures generated without use of orientation restraints

<sup>b</sup> Structure/tensor calculations performed with Cyana by gridsearch; values reported in the table calculated with Amber. <sup>c</sup> Values obtained for calculations in which the structure and orientation tensor were simultaneously optimized using RDCs as restraints

<sup>d</sup> Values obtained for calculations in which the structure and orientation tensor were simultaneously optimized using RDCs and RCSAs as restraints

<sup>e</sup> Values obtained for calculations in which the structure and orientation tensor were simultaneously optimized using RCSAs<sup>f</sup> as restraints

<sup>f</sup> Values correspond to structure shown in Fig. 6e

<sup>g</sup> Values correspond to structure shown in Fig. 6f. The high rhombicity appears inconsistent with the calculated, axially symmetric diffusion tensor (principal components ( $\text{amu}\cdot\text{\AA}^2$ ):  $D_{zz} = 0.59 \times 10^6$ ;  $D_{xx} = 1.52 \times 10^6$ ;  $D_{yy} = 1.54 \times 10^6$ )

range expected on the basis of the X-ray structures. Thus, regardless of whether the force field was modified to favor collapsed or expanded major grooves, inclusion of the RDC and RCSA restraints led to structures with major groove widths compatible with those of the high-resolution X-ray structures (Table 1).

#### Limitation of RCSAs for alignment tensor determination

As indicated above, Amber refinements using RDCs or RDCs and RCSAs as restraints were performed in a manner in which the atomic coordinates and alignment tensors were simultaneously optimized, and in all cases the calculations converged to single solutions with 3D structures and alignment tensors that were generally very similar (Tables 1 and 3, respectively). In contrast, calculations using only the RCSA restraints for simultaneous optimization of the structure and alignment tensor did not afford single structure/tensor solutions. Two representative structures generated by this approach are shown in Fig. 6e and f. Although these structures (and other structures not shown) exhibited similar, low energies upon refinement, the alignment tensors were often significantly different. For example, the wider major groove of the structure shown in Fig. 6e ( $d_{p,p} = 9.7 \pm 0.3 \text{ \AA}$ ) is associated with an alignment tensor that is essentially axially symmetric and similar to those obtained upon refinement using only RDCs ( $A_a$  (axial component of the Saupe alignment tensor) and  $A_r$  (rhombic component) of the alignment tensor =  $119.8 \times 10^{-5}$  and  $1.1 \times 10^{-5}$ , respectively; Table 3), whereas the minimized structure with the collapsed major groove ( $d_{p,p} = 4.5 \pm 0.2 \text{ \AA}$ , Fig. 6f) and high Roll ( $\sim 15^\circ$ ,

Table 1) is associated with a significantly rhombic tensor ( $A_a = 149.8 \times 10^{-5}$ ,  $A_r = 30.2 \times 10^{-5}$ ; Table 3).

The rhombicity of the alignment tensor associated with the collapsed major groove (Fig. 6f; top) is incompatible with both the experimental RDC data (Fig. 6f; bottom) and the calculated diffusion tensor, which is axially symmetric (Table 3 caption). The problem appears to be that, although the number of RCSA restraints employed (36) was similar to the number of restraints used in the RDC-only calculations (42), the information content provided by the RCSAs was lower. This is because the RCSAs associated with a particular nucleotide (i.e., the pyrimidine C<sub>5</sub> and C<sub>6</sub> RCSAs, and the adenosine C<sub>2</sub> and C<sub>8</sub> RCSAs) provide nearly redundant alignment information, due to the fact that the most shielded components of their alignment tensors are almost perpendicular to the plane of the base and nearly parallel to each other (differing by less than  $\sim 30^\circ$ ; Hansen and Al-Hashimi 2006; Ying et al. 2006). Although the redundancy can help reduce biases associated with measurement errors, the angular information content of the RCSA data is essentially half that of the RDC data for A, C and U bases (assuming all aromatic  $^{13}\text{C}$ - $^1\text{H}$  dipolar couplings and the associated  $^{13}\text{C}$  CSAs are available). In addition, the RCSA restraints that were measurable for [DIS]<sub>2</sub> were asymmetrically distributed about the helix axis, and this asymmetry correlated with the rhombicity in the alignment tensors calculated for the highly compressed structures (Figs. 6f, 7). Thus, the inability of RCSAs alone to afford unique structure/alignment tensor solutions, and the calculation of compressed structures with highly rhombic alignment tensors, appears to be due to (a) the reduced amount of unique angular information in the RCSAs (due to nearly redundant CSA orientations) and (b)

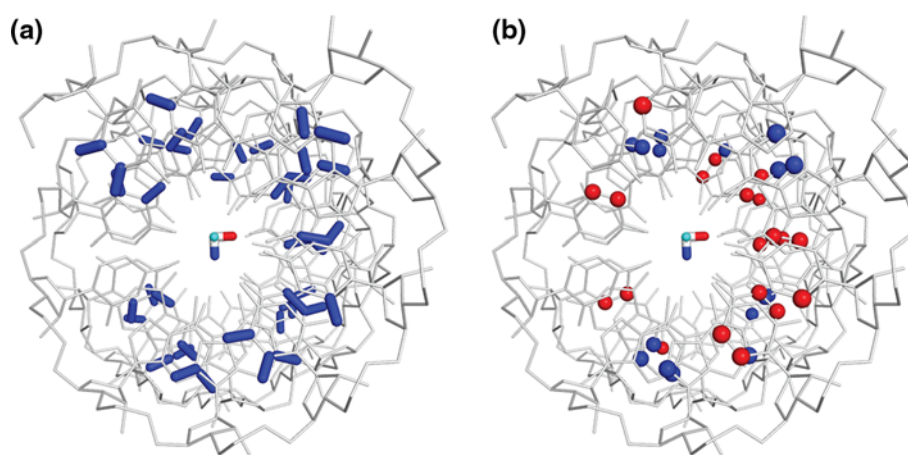


**Fig. 7** Distribution of **a** RDC and **b** RCSA restraints used for structure calculations; RNA in gray,  $^{13}\text{C}$ - $^1\text{H}$  vectors shown as blue sticks,  $^{13}\text{C}$  RCSAs for purines and pyrimidines shown as spheres (blue and red, respectively). The structure corresponds to that shown in Fig. 5f, which was calculated using only RCSA restraints and has a

collapsed major groove. The eigenvectors of the Saupe alignment tensor are also shown ( $zz = \text{cyan}$ ,  $xx = \text{red}$ ,  $yy = \text{blue}$ ; eigenvalues  $|zz|:|xx|:|yy| \approx 3:2:1$ ). The rhombicity of the tensor relative to the helix axis in this structure correlates with the asymmetric restraint distribution (see text)

asymmetric distribution of the restraints employed. It is important to note, however, that once the alignment tensor of  $[\text{DIS}]_2$  had been established from the RDC or RDCs+RCSA data, the RCSA restraints alone afforded structures that were very similar to those calculated with the RDC or RDC+RCSA restraints, even when a highly deficient force field was employed (Table 1).

## Conclusions

An assessment of A-form helical RNA structures determined by high resolution X-ray crystallography and NMR revealed systematic differences, the most notable being the significantly larger major groove widths of a majority of the NMR structures. As commonly employed, NOE-derived distance, dihedral angle, and hydrogen bonding restraints are compatible with a wide range of A-like conformations, and as such, structures generated using only these restraints are sensitive to the force fields employed during refinement.  $[\text{DIS}]_2$  structures calculated with Cyana using loose distance restraints afforded structures with collapsed major grooves, due to the fact that the restraints correspond predominantly to distances within the major groove. Refinement with the Amber ff99 force field with GB solvent continuum parameters afforded  $[\text{DIS}]_2$  structures with features that more closely resembled those observed in high-resolution X-ray structures (compared with those calculated with Cyana), except that the major groove widths were  $\sim 2$  Å wider than expected. The application of orientation restraints derived from either aromatic  $^1\text{H}$ - $^{13}\text{C}$  RDCs or  $^{13}\text{C}$  RCSAs resulted in structures with helical properties consistent with those observed in the surveyed X-ray crystal structures, not only when conducted with the standard Amber force field, but also when performed with altered force fields that favor both wider and narrower major groove widths. In particular, the major groove  $d_{\text{P-P}}$  distances calculated with RDC and RCSA restraints ( $11 \pm 1$  Å) are fully consistent with those observed in the surveyed X-ray structures.

Empirical methods have been employed in the past to overcome experimental restraint limitations, including the use of database potentials based on statistical analyses of torsion angles and base-to-base positions in RNA X-ray crystal structures (Clare and Kuszewski 2003), the use of loose inter-phosphate distance restraints using X-ray structures as a guide (D'Souza et al. 2004), and the empirical tuning of force field terms (Rife et al. 1999). Such empirical adjustments and/or restraints were not required to obtain X-ray compatible structures of  $[\text{DIS}]_2$ . Although it is currently not possible to know the “true” solution structure, the fact that the refined structures provide better fits to two classes of experimental data (RDCs

and RCSAs) provides good evidence that they more accurately represent the actual solution state conformation.

The simultaneous fitting of the atomic coordinates and alignment tensor to the RCSA data afforded multiple solutions, many of which were incompatible with the RDC data and the calculated diffusion tensor. Because the  $^{13}\text{C}$  CSA tensors of a given nucleotide sample similar angular space relative to the alignment tensor, the information content available from the RCSA data is comparatively lower than that of the RDC data. Thus, the use of RCSAs alone for simultaneous structure/tensor determination should probably be avoided for systems similar to  $[\text{DIS}]_2$ . However, the redundancies can be useful for overcoming errors associated with uncertainties in signal frequency measurement, and when employed with RDCs or independently using a pre-determined alignment tensor, RCSAs provide additional restraint information consistent with that provided by the RDCs.

The IMC pulse sequence presented here provides a sensitive approach for measuring individual  $^1\text{H}$ - $^{13}\text{C}$  multiplet component frequencies for aromatic C-H groups in  $^{13}\text{C}$ -labeled RNA. When combined with RPCSA data,  $^1\text{H}$ - $^{13}\text{C}$  RDCs can be measured directly, providing a convenient means for calculating aromatic  $^{13}\text{C}$  RCSAs. The approach is readily applicable to RNAs as large as 50 nt, and should be applicable to RNAs with correlation times as long as  $\sim 10$  ns (Grishaev et al. 2006).

## Methods

### Sample preparation

RNA samples were prepared by in vitro transcription using T7 RNA polymerase and synthetic DNA templates that were 2'-O-methylated at the first and second base positions to prevent N+1 addition (Kao et al. 1999). To increase RNA yield by preventing the accumulation of insoluble Mg-PPi complexes, reactions were supplemented with Yeast Inorganic Pyrophosphatase (New England Biolabs) at a final concentration of  $\sim 1$  unit/mL. Transcriptions were carried out in 20 ml reaction volumes using fully protonated ribonucleotide triphosphates (rNTPs; Sigma) or  $^{13}\text{C}$  specifically labeled rNTPs (Spectra Stable Isotopes, Columbia MD). Following synthesis, the RNAs were chloroform-phenol extracted, ethanol precipitated, and purified to homogeneity on 20% preparative denaturing PAGE gels. RNA fragments were electroeluted and desalted using Amersham NAP-25 columns, washed three times with NaCl (2 M, 5x(v/v)), then washed eight times with purified water (Millipore, 5x(v/v)). Samples were dialyzed against 10 mM Tris pH 7.5, 150 mM NaCl, lyophilized and re-suspended in either 100%  $\text{D}_2\text{O}$  or 90%  $\text{H}_2\text{O}/10\%$   $\text{D}_2\text{O}$ . Some chemical

shifts were sensitive to small variations in sample pH and ionic strength, and samples for RDC/RCSA measurements were prepared by simultaneous dialysis against a common buffer reservoir using microscale dialysis buttons (Hampton Research, Aliso Viejo, CA). Final RNA concentrations ranged from 0.5 to 1.5 mM (120  $\mu$ L in 3 mm NMR sample tubes (Shigemi Inc., Japan)). Filamentous Pf1 phage (Asla Biotech Ltd, Riga, Latvia) concentrations were determined from the  $^2\text{H}$  quadrupolar splittings of the  $\text{D}_2\text{O}$  signal (Hansen et al. 1998).

### NMR spectroscopy

NMR spectra were recorded on Bruker Avance (800 MHz) or DMX (600 MHz) instruments both equipped with triple-resonance 5 mm cryogenic probes and containing a z-axis pulsed field gradient accessory. NMR data were processed with NMRPipe/NMRDraw (Delaglio et al. 1995) and analyzed using NMRView (Johnson and Blevins 1994). Non-exchangeable  $^1\text{H}$  assignments were made from 2D NOESY (200 ms mixing time; Jeener et al. 1979; Macura and Ernst 1980) and 2D TOCSY (75 ms mixing time; Griesinger et al. 1988) spectra recorded at 303 K.  $^{13}\text{C}$  chemical shift assignments were made by comparing  $^1\text{H}$ - $^{13}\text{C}$  HMQC (Bax and Subramanian 1986) and TROSY-HSQC (Pervushin et al. 1997) spectra, obtained for samples with nucleotide-specific  $^{13}\text{C}$ -labeling, with the assigned 2D NOESY spectrum. Exchangeable  $^1\text{H}$  assignments were made at 298 K using the Watergate-NOESY (200 ms mixing time) pulse sequence (Piotto et al. 1992). Proton resonance assignments were made by standard sequential assignment methods (Wüthrich 1986).

One bond  $^1\text{J}_{\text{CH}}$  (and  $^1\text{D}_{\text{CH}}$ ) and  $^{13}\text{C}$  chemical shifts were measured from NMR spectra obtained using a modified form of the  $^{13}\text{C}$ -decoupled RPCSA pulse sequence (Grishaev et al. 2006; called the IMC pulse sequence, Fig. 2a). The phases of the final  $^{13}\text{C}$  rf pulse ( $\phi_7$ ) and TROSY back-transfer  $^1\text{H}$  rf pulse ( $\phi_8$ ) were adjusted to specifically detect the desired component of the  $^{13}\text{C}$ - $\{^1\text{H}\}$  doublet. The phase of the final  $^{13}\text{C}$  pulse ( $\phi_7$ ) was empirically adjusted ( $-38^\circ$ ) to eliminate the spurious signals from the unwanted coherence pathways, which arise due to differential relaxation rates of single and multiple quantum coherence. RPCSA spectra were obtained as a reference to account for potential (minor)  $^1\text{H}$  NMR chemical shift changes that can occur as a function of added alignment media (the pulse sequence and parameters are available from the original authors upon request (Grishaev et al. 2006)). Three separate sets of spectra (obtained using optimized  $^1\text{H}$  and  $^{13}\text{C}$  decoupling pulses) were generated for measurement of  $\text{C}_2\text{-H}_2$ ,  $\text{C}_{6/8}\text{-H}_{6/8}$ , and  $\text{C}_5\text{-H}_5$  correlations. RPCSA ( $\Delta\delta'$ ) values were determined by taking the difference in the  $^{13}\text{C}$  chemical shift under

aligned ( $\delta'_{\text{aniso}}$ ) and isotropic ( $\delta'_{\text{iso}}$ ) conditions. Prior to calculation of  $\Delta\delta'$ , the  $\delta'_{\text{aniso}}$  shifts were corrected to account for the change in lock frequency resulting from the  $^2\text{H}$  quadrupolar splitting (Hansen and Al-Hashimi 2006; Ying et al. 2006). RCSAs ( $\Delta\delta$ ) were subsequently calculated based on the relationship:  $\Delta\delta_{\text{Hz}} = \Delta\delta'_{\text{Hz}} - \text{RDC}/2$ .

IMC data for purines were collected in two sets of experiments, with the  $^1\text{H}$  and  $^{13}\text{C}$  rf frequencies centered in the  $\text{H}_8/\text{C}_8$  and  $\text{H}_2/\text{C}_2$  regions of the spectra. IMC spectra for the  $\text{H}_5/\text{C}_5$  and  $\text{H}_6/\text{C}_6$  correlations of pyrimidines were collected similarly, except that for  $\text{C}_6/\text{H}_6$  data collection, the  $^{13}\text{C}$  broad band hyperbolic secant and selective IBURP inversion pulses, and selective  $^1\text{H}$  IBURP inversion pulse, were centered on the  $^{13}\text{C}_5$  and  $^1\text{H}_5$  frequencies, respectively (and vice versa).

### Implementation of RCSA restraints in Amber

The Amber restrained dynamics calculations include a penalty function ( $E_{\text{CSA}} = k_{\text{CSA}}(\Delta\delta_{\text{calc}} - \Delta\delta_{\text{obs}})^2$ ), which compares calculated and observed residual CSA values. Implementation involves transforming previously determined  $^{13}\text{C}$  CSA tensors (Ying et al. 2006) from a local coordinate system defined by base pair atoms into the same molecular coordinate frame used for the alignment tensor (see supplementary materials for implementation details). These penalty terms are added to those arising from RDCs, and used for simultaneous refinement of the structure and the alignment tensor elements, as described (Tsui et al. 2000).

### Structure calculations

Structure calculations were performed with a 160 processor Apple Xserve cluster equipped with a low-latency Miracom switch (Apple, Inc., Cupertino CA). Initial structures were generated with Cyana (Güntert et al. 1997; version 2.1) using  $^1\text{H}$ - $^1\text{H}$  distance restraints of 2.7, 3.3 and 5.0  $\text{\AA}$  corresponding to experimentally observed NOEs of strong, medium, and weak intensity, respectively. Upper distance restraints of 4.2  $\text{\AA}$  and 3.2  $\text{\AA}$  were employed for intrasidue  $\text{H}_{8/6}$  to  $\text{H}_3'$  (strong intensity) and  $\text{H}_2'$  (medium intensity) NOEs, respectively, to avoid over-restraining these interactions (D'Souza et al. 2004).

All Amber (version 10; Case et al. 2005) calculations were conducted with the ff99 force field using a generalized Born solvent continuum model (Hawkins et al. 1995; Hawkins et al. 1996; Tsui and Case 2001; Amber igb parameter = 1). Parabolic torsion angle restraints (single-value minimum, 10.0 Mcal/mol-rad $^2$ ) were employed to enforce planarity of the aromatic rings and ideality of covalent angles associated with the glycosidic bonds, which otherwise could exhibit unrealistic deviations during

refinement with RDC and RCSA restraints. Application of RDC/RCSA restraint ranges, estimated from uncertainties in signal frequency measurements, almost always resulted in structures with back-calculated RDC and RCSA values at their prescribed boundary limits. This was due to the fact that the restraints opposed terms in the Amber force field that promoted wide (normal or twofold enhanced electrostatic term) or narrow (90% reduced electrostatic term) major grooves, and as such, similar degrees of convergence were obtained using loose (non-single value) orientation restraints. For this reason, the RDCs and RCSAs were implemented as single-value minima restraints, which were allowed to deviate during the calculations by applying relatively soft RDC and RCSA weighting coefficients (0.1). Cyana structures with lowest target functions were subjected to 1,000 steps of unrestrained conjugate gradient minimization (CGM; 12 Å non-bonded force cut off) to remove possible bad contacts, prior to restrained MD simulations.

The CGM minimized Cyana structures were subjected to MD simulations under two different sets of conditions: one using the standard Amber force field, and the other using a force field with the weighting coefficient for electrostatic interactions ( $E_{\text{elec}}$ ) reduced to 10% of the standard value. Structures were initially refined without the use of the NOE-derived distance restraints, but for comparison with subsequent calculations, chirality and H-bond restraints were also employed. Structures with added NOE-derived distance restraints were heated to either 50 K or 350 K prior to equilibration at 0 K (400,000 steps per MD simulation, 0.2 fs/step; salt concentration = 150 mM). Since essentially identical results were obtained for the 50 K and 350 K calculations, all subsequent calculations were performed at 50 K.

MD simulations were then performed using the following combinations of experimental restraints: distance + RDC restraints, distance + RDC + RCSA restraints, distance + RCSA restraints. Calculations were initially conducted with fixed atomic coordinates to generate an initial alignment tensor (100,000 steps minimization). Structures were then heated from 0 to 50 K (40,000 steps, 0.2 fs/step), maintained at 50 K (60,000 steps), slowly cooled to 0 K (200,000 steps), then maintained at 0 K (200,000 steps) using the different combinations of NOE-derived distance and orientation restraints described above. Penalty energies were most evenly distributed among the experimental restraints using RDC and RCSA penalty weight coefficients of 0.1.

Idealized coordinates for  $[\text{DIS}]_2$  were generated with Nucgen (Bansal et al. 1995) and equilibrated at 0 K using the protocol employed for the Cyana structures. Calculations were performed using the standard Amber force field with only chirality and H-bond restraints.

For comparison purposes, alignment tensors for the Cyana and Nucgen structures, and the Amber structures generated without orientation restraints, were calculated by Amber minimization (100,000 steps) using fixed atom positions. Back-calculated RDC and RCSA values obtained by this approach were similar to those obtained using RAMAH (Hansen and Al-Hashimi 2006). The axial and rhombic components of the alignment tensors are reported as  $A_a = (|lzz|)/2$  and  $A_r = (|lxx| - |lyy|)/3$ , respectively, where the eigenvalues of the alignment matrix are ordered as  $|lzz| > |lyy| > |lxx|$ .

Structural parameters were assessed using X3DNA (Lu and Olson 2003; Lu and Olson 2008), interphosphate distance measurements and figures of structures were made with PyMOL (DeLano 2002), and quality assessments were made with Molprobit (Davis et al. 2007).

**Acknowledgments** Support from the NIH (GM42561 to M.F.S., GM45811 to D.A.C.) and the Intramural Research Program of the NIDDK, NIH (DK029051-03 to A.B.) is gratefully acknowledged. B.K., P.S., S.B. and R.S. are UMBC Meyerhoff Scholars and were supported by an HHMI undergraduate education grant.

## References

- Al-Hashimi HM (2007) Beyond static structures of RNA by NMR: folding, refolding, and dynamics at atomic resolution. *Biopolymers* 86:345–347
- Al-Hashimi HM, Patel DJ (2002) Residual dipolar couplings: synergy between NMR and structural genomics. *J Biomol NMR* 22:1–8
- Al-Hashimi HM, Walter NG (2008) RNA dynamics: it is about time. *Curr Opin Struct Biol* 18:321–329
- Al-Hashimi HM, Gorin A, Majumdar A, Patel DJ (2001a) Alignment of the HTLV-I Rex peptide bound to its target RNA aptamer from magnetic field-induced residual dipolar couplings and intermolecular hydrogen bonds. *J Am Chem Soc* 123:3179–3180
- Al-Hashimi HM, Majumdar A, Gorin A, Kettani A, Skripkin E, Patel DJ (2001b) Field- and phage-induced dipolar couplings in a homodimeric DNA quadruplex: relative orientation of G. (C-A) triad and G-tetrad motifs and direct determination of C2 symmetry axis orientation. *J Am Chem Soc* 123:633–640
- Al-Hashimi HM, Tolman JR, Majumdar A, Gorin A, Patel DJ (2001c) Determining stoichiometry in homomultimeric nucleic acid complexes using magnetic field induced residual dipolar couplings. *J Am Chem Soc* 123:5806–5807
- Al-Hashimi HM, Gosser Y, Gorin A, Hu W, Majumdar A, Patel DJ (2002) Concerted motions in HIV-1 TAR RNA may allow access to bound state conformations: RNA dynamics from NMR residual dipolar couplings. *J Mol Biol* 315:95–102
- Al-Hashimi HM, Pitt SW, Majumdar A, Xu W, Patel DJ (2003) Mg<sup>2+</sup>-induced variations in the conformation and dynamics of HIV-1 TAR RNA probed using NMR residual dipolar couplings. *J Mol Biol* 329:867–873
- Allain FH-T, Varani G (1997) How accurately and precisely can RNA structure be determined by NMR? *J Mol Biol* 267:338–351
- Andersson P, Annala A, Otting G (1998) An alpha/beta-HSQC-alpha/beta experiment for spin-state selective editing of IS cross peaks. *J Magn Reson* 133:364–367

- Bansal M, Bhattacharyya D, Ravi B (1995) NUPARM and NUCGEN: software for analysis and generation of sequence dependent nucleic acid structures. *Comput Appl Biosci* 11:281–287
- Bax A, Grishaev A (2005) Weak alignment NMR: a hawk-eyed view of biomolecular structure. *Curr Opin Struct Biol* 15:563–570
- Bax A, Subramanian S (1986) Sensitivity-enhanced two-dimensional heteronuclear shift correlation NMR spectroscopy. *J Magn Reson* 67:565–569
- Bayer P, Varani L, Varani G (1999) Refinement of the structure of protein-RNA complexes by residual dipolar coupling analysis. *J Biomol NMR* 14:149–155
- Brutscher B, Boisbouvier J, Pardi A, Marion D, Simorre JP (1998) Improved sensitivity and resolution in  $1\text{H}$ – $^{13}\text{C}$  NMR experiments of RNA. *J Am Chem Soc* 120:11845–11851
- Bryce DL, Grishaev A, Bax A (2005) Measurement of ribose carbon chemical shift tensors for A-form RNA by liquid crystal NMR spectroscopy. *J Am Chem Soc* 127:7387–7396
- Case DA et al (2005) The Amber biomolecular simulation programs. *J Computat Chem* 26:1668–1688
- Clore GM, Kuszewski J (2003) Improving the accuracy of NMR structures of RNA by means of conformational database potentials of mean force as assessed by complete dipolar coupling cross-validation. *J Am Chem Soc* 125:1518–1525
- D'Souza V, Melamed J, Habib D, Pullen K, Wallace K, Summers MF (2001) Identification of a high-affinity nucleocapsid protein binding site within the Moloney Murine Leukemia Virus  $\Psi$ -RNA packaging signal. Implications for genome recognition. *J Mol Biol* 314:217–232
- D'Souza V, Dey A, Habib D, Summers MF (2004) NMR structure of the 101 nucleotide core encapsidation signal of the Moloney Murine Leukemia Virus. *J Mol Biol* 337:427–442
- Davis JH, Tonelli M, Scott LG, Jaeger L, Williamson JR, Butcher SE (2005) RNA helical packing in solution: NMR structure of a 30 kDa GAAA tetraloop-receptor complex. *J Mol Biol* 351:371–382
- Davis IW et al (2007) MolProbity: all-atom contacts and structure validation for proteins and nucleic acids. *Nucleic Acids Res* 35:W375–W383
- Delaglio F, Grzesiek S, Vuister GW, Zhu G, Pfeifer J, Bax A (1995) NMRPipe: a multidimensional spectral processing system based on UNIX pipes. *J Biomol NMR* 6:277–293
- DeLano WL (2002) The PyMOL molecular graphics system. DeLano Scientific, San Carlos
- Dock-Bregeon AC, Chevrier B, Podjarny A, Johnson J, De Bear JS, Gough GR, Gilham PT, Moras D (1989) Crystallographic structure of an RNA helix:  $[\text{U}(\text{UA})_6\text{A}]_2$ . *J Mol Biol* 209:459–474
- Fisher CK, Al-Hashimi HM (2009) Approximate reconstruction of continuous spatially complex domain motions by multialignment NMR residual dipolar couplings. *J Phys Chem B* 113:6173–6176
- Frank AT, Stelzer AC, Al-Hashimi HM, Andricioaei I (2009) Constructing RNA dynamical ensembles by combining MD and motionally decoupled NMR RDCs: new insights into RNA dynamics and adaptive ligand recognition. *Nucleic Acids Res* 37:3670–3679
- Green H, Freeman R (1991) Band-selective radiofrequency pulses. *J Magn Reson* 93:93–141
- Griesinger C, Otting G, Wüthrich K, Ernst RR (1988) Clean TOCSY for  $^1\text{H}$  spin system identification in macromolecules. *J Am Chem Soc* 110:7870–7872
- Grishaev A, Ying J, Bax A (2006) Pseudo-CSA restraints for NMR refinement of nucleic acid structures. *J Am Chem Soc* 128:10010–10011
- Gueron M, Leroy LJ, Griffey RH (1983) *J. Am Chem Soc* 105:7262–7266
- Güntert P, Mumenthaler C, Wüthrich K (1997) Torsion angle dynamics for protein structure calculations with a new program. *DYANA J Mol Biol* 273:283–298
- Hansen AL, Al-Hashimi HM (2006) Insight into the CSA tensors of nucleobase carbons in RNA polynucleotides from solution measurements of residual CSA: towards new long-range orientational constraints. *J Magn Reson* 179:299–307
- Hansen MR, Mueller L, Pardi A (1998) Tunable alignment of macromolecules by filamentous phage yields dipolar coupling interactions. *Nat Struct Biol* 5:1065–1074
- Hawkins GD, Cramer CJ, Truhlar DG (1995) Pairwise solute descreening of solute charges from a dielectric medium. *Chem Phys Lett* 246:122–129
- Hawkins GD, Cramer CJ, Truhlar DG (1996) Parameterized models of aqueous free energies of solvation based pairwise descreening of solute atomic charges from a dielectric medium. *J Phys Chem* 100:19824–19839
- Jeener J, Meier BH, Bachmann P, Ernst RR (1979) Investigation of exchange processes by two-dimensional NMR spectroscopy. *J Chem Phys* 71:4546–4553
- Johnson BA, Blevins RA (1994) NMRview: a computer program for the visualization and analysis of NMR data. *J Biomol NMR* 4:603–614
- Kao C, Zheng M, Rüdiger S (1999) A simple and efficient method to reduce nontemplated nucleotide addition at the 3 terminus of RNAs transcribed by T7 RNA polymerase. *RNA* 5:1268–1272
- Kim NK, Zhang Q, Zhou J, Theimer CA, Peterson RD, Feigon J (2008) Solution structure and dynamics of the wild-type pseudoknot of human telomerase RNA. *J Mol Biol* 384:1249–1261
- Klein DJ, Moore PB, Steitz TA (2004) The roles of ribosomal proteins in the structure assembly, and evolution of the large ribosomal subunit. *J Mol Biol* 340:141–177
- Klosterman E, Shah SA, Steitz S (1999) Crystal structures of two plasmid copy control related RNA duplexes: an 18 base pair duplex at 1.20 Å resolution and a 19 base pair duplex at 1.55 Å resolution. *Biochemistry* 38:14784–14792
- Latham MP, Hanson P, Brown DJ, Pardi A (2008) Comparison of alignment tensors generated for native tRNAVal using magnetic fields and liquid crystalline media. *J Biomol NMR* 40:83–94
- Lawrence DC, Stover CC, Noznitsky J, Wu Z-R, Summers MF (2003) Structure of the intact stem and bulge of HIV-1  $\Psi$ -RNA stem loop SL1. *J Mol Biol* 326:529–542
- Leonard GA, McAuley-Hecht KE, Ebel S, Lough DM, Brown T, Hunter WN (1994) Crystal and molecular structure of r(CGCGAAUUAGCG): an RNA duplex containing two G(anti).A(anti) base pairs. *Structure* 2:483–494
- Lu X-J, Olson WK (2003) 3DNA: a software package for the analysis, building and visualization of three-dimensional nucleic acid structures. *Nucl Acids Res* 31:5108–5121
- Lu X-J, Olson WK (2008) 3DNA: a versatile, integrated software system for the analysis, rebuilding and visualization of three-dimensional nucleic acid structures. *Nature Prot* 3:1213–1227
- Lukavsky PJ, Puglisi JD (2005) Structure determination of large biological RNAs. *Methods Enzymol* 394:399–415
- Lukavsky PJ, Kim I, Otto GA, Puglisi JD (2003) Structure of HCV IRES domain II determined by NMR. *Nature Struct Biol* 10:1033–1038
- Macura S, Ernst RR (1980) Elucidation of cross relaxation in liquids by two-dimensional NMR spectroscopy. *Mol Phys* 41:95–117
- Mollova ET, Hansen MR, Pardi A (2000) Global structure of RNA determined with residual dipolar couplings. *J Am Chem Soc* 122:11561–11562
- Pan ZW, Mitra SN, Sundaralingam M (1998) Structure of a 16-mer RNA duplex r(GCAGACUUAAAUCUGC) $_2$  with wobble C.A+ mismatches. *J Mol Biol* 283:977–984

- Pervushin K, Riek R, Wider G, Wüthrich K (1997) Attenuated T2 relaxation by mutual cancellation of dipole-dipole coupling and chemical shift anisotropy indicates an avenue to NMR structures of very large biological macromolecules in solution. *Proc Natl Acad Sci USA* 94:12366–12371
- Piotto M, Saudek V, Sklenar V (1992) Gradient-tailored excitation for single-quantum NMR spectroscopy of aqueous solutions. *J Biomol NMR* 2:661–665
- Rife JP, Stallings SC, Correll CC, Dallas A, Steitz TA, Moore PB (1999) Comparison of the crystal and solution structures of two RNA oligonucleotides. *Biophys J* 76:66–75
- Saenger W (1984) *Principles of nucleic acid structure*. Springer, New York
- Shah SA, Brunger AT (1999) The 1.8 Å crystal structure of a statically disordered 17 base pair RNA duplex: principles of RNA crystal packing and its effect on nucleic acid structure. *J Mol Biol* 285:1577–1588
- Skrisovska L et al (2007) The testis-specific human protein RBMY recognizes RNA through a novel mode of interaction. *EMBO Rep* 8:372–379
- Staple DW, Butcher SE (2005) Solution structure and thermodynamic investigation of the HIV-1 frameshift inducing element. *J Mol Biol* 349:1011–1023
- Steff R, Wu H, Ravindranathan S, Sklenar V, Feigon J (2004) DNA A-tract bending in three dimensions: solving the dA4T4 vs. dT4A4 conundrum. *Proc Natl Acad Sci USA* 101:1177–1182
- Tjandra N, Tate S, Ono A, Kainosho M, Bax A (2000) The NMR structure of a DNA dodecamer in an aqueous dilute liquid crystalline phase. *J Am Chem Soc* 122:6190–6200
- Trantirek L, Urbasek M, Steff R, Feigon J, Sklenar V (2000) A method for direct determination of helical parameters in nucleic acids using residual dipolar couplings. *J Am Chem Soc* 122:10454–10455
- Trikha J, Filman DJ, Hogle JM (1999) Crystal structure of a 14 bp RNA duplex with non-symmetrical tandem GxU wobble base pairs. *Nucleic Acids Res* 27:1728–1739
- Tsui V, Case DA (2001) Theory and applications of the generalized Born solvation model in macromolecular simulations. *Biopolymers* 2001:275–291
- Tsui V, Zhu L, Huang TH, Wright PE, Case DA (2000) Assessment of zinc finger orientations by residual dipolar coupling constants. *J Biomol NMR* 16:9–21
- Walsh JD, Wang YX (2005) Periodicity, planarity, residual dipolar coupling, and structures. *J Magn Reson* 174:152–162
- Walsh JD, Cabello-Villegas J, Wang YX (2004) Periodicity in residual dipolar couplings and nucleic acid structures. *J Am Chem Soc* 126:1938–1939
- Wang J, Walsh JD, Kuszewski J, Wang YX (2007) Periodicity, planarity, and pixel (3P): a program using the intrinsic residual dipolar coupling periodicity-to-peptide plane correlation and phi/psi angles to derive protein backbone structures. *J Magn Reson* 189:90–103
- Warren JJ, Moore PB (2001) Application of dipolar coupling data to the refinement of the solution structure of the sarcin-ricin loop RNA. *J Biomol NMR* 20:311–323
- Werbelow LG, Grant DM (1977) Carbon-13 NMR relaxation and molecular dynamics: overall movement and internal rotation of methyl groups in N,N-dimethylformamide. *Adv Magn Reson* 9:189–299
- Wüthrich K (1986) *NMR of proteins and nucleic acids*. Wiley, New York
- Ying J, Grishaev A, Bryce DL, Bax A (2006) Chemical shift tensors of protonated base carbons in helical RNA and DNA from NMR relaxation and liquid crystal measurements. *J Am Chem Soc* 128:11443–11454
- Ying J, Grishaev A, Latham MP, Pardi A, Bax A (2007) Magnetic field induced residual dipolar couplings of imino groups in nucleic acids from measurements at a single magnetic field. *J Biomol NMR* 39:91–96
- Zhang Q, Al-Hashimi HM (2008) Extending the NMR spatial resolution limit for RNA by motional couplings. *Nat Methods* 5:243–245
- Zhang Q, Sun X, Watt ED, Al-Hashimi HM (2006) Resolving the motional modes that code for RNA adaptation. *Science* 311:653–656
- Zhang Q, Stelzer AC, Fisher CK, Al-Hashimi HM (2007) Visualizing spatially correlated dynamics that directs RNA conformational transitions. *Nature* 450:1263–1267
- Zhou H, Vermeulen A, Jucker FM, Pardi A (2001) Incorporating residual dipolar couplings into the NMR structure determination of nucleic acids. *Biopolymers* 52:168–180
- Zuo X et al (2008) Global molecular structure and interfaces: Refining an RNA:RNA complex structure using solution X-ray scattering data. *J Am Chem Soc* 130:3292–3293